

Reaction and proton-removal cross sections of ${}^6\text{Li}$, ${}^7\text{Be}$, ${}^{10}\text{B}$, ${}^{9,10,11}\text{C}$, ${}^{12}\text{N}$, ${}^{13,15}\text{O}$ and ${}^{17}\text{Ne}$ on Si at 15 to 53 MeV/nucleon

R. E. Warner

Oberlin College, Oberlin, Ohio 44074

F. Carstoiu,

*Cyclotron Institute, Texas A & M University, College Station, Texas 77843 and
IFIN-HH, 76900 Bucharest-Magurele, Romania*

J. A. Brown

Wabash College, Crawfordsville, Indiana 47933

F. D. Becchetti and D. A. Roberts

University of Michigan, Ann Arbor, Michigan 48109

B. Davids

TRIUMF, 4004 Wesbrook Mall, Vancouver, Canada, V6T 2A3

A. Galonsky, R. M. Ronningen, and M. Steiner

National Superconducting Cyclotron Laboratory, East Lansing, Michigan 48824

M. Horoi

Department of Physics, Central Michigan University, Mount Pleasant, Michigan 48859

J. J. Kolata

University of Notre Dame, Notre Dame, Indiana 46556

A. Nadasen

University of Michigan, Dearborn, Michigan 48128

C. Samanta

*Virginia Commonwealth University, Richmond, Virginia 23284 and
Saha Institute of Nuclear Physics, 1/AF, Bidhannagar, Kolkata 700064*

J. Schwarzenberg

Institute of Nuclear Physics, University of Vienna, Waehringerstrasse 17, A-1090, Vienna, Austria

K. Subotic

Institute of Nuclear Sciences, VINCA, Belgrade 11001, Yugoslavia

(Dated: July 7, 2018)

Excitation functions for total reaction cross sections, σ_R , were measured for the light, mainly proton-rich nuclei ${}^6\text{Li}$, ${}^7\text{Be}$, ${}^{10}\text{B}$, ${}^{9,10,11}\text{C}$, ${}^{12}\text{N}$, ${}^{13,15}\text{O}$, and ${}^{17}\text{Ne}$ incident on a Si telescope at energies between 15 and 53 MeV/nucleon. The telescope served as target, energy degrader and detector. Proton-removal cross sections, σ_{2p} for ${}^{17}\text{Ne}$ and σ_p for most of the other projectiles, were also measured. The strong absorption model reproduces the A -dependence of σ_R , but not the detailed structure. Glauber multiple scattering theory and the JLM folding model provided improved descriptions of the measured σ_R values. *rms* radii, extracted from the measured σ_R using the optical limit of Glauber theory, are in good agreement with those obtained from high energy data. One-proton removal reactions are described using an extended Glauber model, incorporating second order noneikonal corrections, realistic single particle densities, and spectroscopic factors from shell model calculations.

PACS numbers: 24.10.-i, 25.60.-t, 25.60.Dz, 25.60.Gc, 25.70.Mn

I. INTRODUCTION

The interesting properties of radioactive nuclei produced in the laboratory include their lifetimes, sizes and

distributions of nuclear matter, shell structure, excited states, and decay modes. Often, the one-particle separation energies are small, of the order of 1 MeV or less.

These small separation energies lead to a wealth of phenomena including soft collective modes, exotic transition strengths between low-lying states, changes in shell structure, long-tailed density distributions, and, perhaps most dramatically, halo nuclei. In one-particle removal reactions, the parallel and transverse momentum distributions of the core-like fragments are very narrow as compared with those of normal nuclei, indicating increased nuclear size. The total reaction and breakup cross sections are large, also reflecting the increased nuclear size. Spontaneous $2p$ radioactivity has been observed recently near the proton drip line [1, 2]. The increased density in the tails of the matter distribution generates a competition between the increased refractive power of the real optical potential and the increased absorption due to the imaginary part, leading to exotic shapes in heavy ion elastic scattering angular distributions.

Total reaction cross sections, σ_R , and proton-removal cross sections, σ_p , contain complementary information about the size and matter distributions of atomic nuclei. Various reactions at all impact parameters contribute to σ_R , which therefore reflects mainly the *rms* nuclear radius. Breakup, however, is a peripheral process, hence σ_p is sensitive mainly to the surface distribution. Therefore these combined data are needed to better describe the matter distribution, and the best test of theory is obtained by fitting them simultaneously.

Measurements of both σ_R and σ_p can be used to identify proton-halo nuclei. Among the light nuclei, ^8B has been identified as a proton-halo nucleus. The evidence includes its enhanced σ_R at low energies [3], as well as a narrow longitudinal momentum distribution of the ^7Be core following proton removal. [4, 5, 6]

We report σ_R measurements for the stable and short-lived light nuclei ^6Li , ^7Be , ^{10}B , $^{9,10,11}\text{C}$, ^{12}N , $^{13,15}\text{O}$, and ^{17}Ne incident on Si targets at energies ranging from 15 to 53 MeV/nucleon. Most of these nuclei are proton-rich; some are on the proton drip line, and therefore may be proton-halo candidates. The measurements were made by aiming these projectiles at a stack of thin Si elements which served as both targets and detectors. We also report σ_p for most of the projectiles, the exceptions being ^9C , whose σ_p we previously reported [7], and ^6Li and ^{10}C , which are unbound following single proton removal. We report σ_{2p} for the 2-proton-halo candidate ^{17}Ne [8], which is also unbound after p-removal. A preliminary account of this experiment appeared earlier [9]. Those data are superseded by the present measurements since we have now more effectively identified and rejected the unwanted components of the beams used in the experiment.

Proton and heavy ion radiotherapy is now utilized in the treatment of cancer [10]. These beams produce nuclear fragments, including short-lived isotopes such as ^{11}C , and these can contribute significant dosage. Experimental σ_R data are needed for both stable and short-lived light ions to better quantify both the dosage delivered by these fragments and their spatial distribution along the

beam path.

We interpret our data using phenomenological strong absorption models, as well as more elaborate models such as the optical limit of Glauber multiple-scattering theory. Breakup reactions are described in an extended Glauber model, incorporating second order noneikonal corrections and shell model spectroscopic factors, as well as double folding optical potentials generated by complex, density-dependent and energy-dependent nucleon-nucleon (NN) effective interactions.

Section II of this paper describes the beams, target-detector system, and procedure utilized for the measurements. Section III explains the selection of reaction events and the methods used to determine σ_R and σ_p . The theoretical calculations are presented and compared with our data in Section IV. Section V briefly summarizes our results and the conclusions we draw.

II. THE EXPERIMENT

Our measurements of σ_R are similar to those made earlier for the He and Li isotopes on Si [11]. Collimated monoenergetic projectiles are selected in a multi-detector Si telescope. Reaction events are then identified as those whose total energy loss in the telescope differs from that of non-reacting projectiles. Since the projectile's energy decreases as it travels through the telescope, we obtained cross sections at different energies by identifying the detector in which a reaction occurred; i.e., the first detector to give a signal different from projectile signals.

To measure σ_p , the heavy fragments from proton removal reactions were observed in particle identification spectra from two detectors – the one which stops the fragment and the one which precedes it – following those in which the breakup reactions occur [7].

An 80 MeV/nucleon ^{20}Ne beam at the National Superconducting Cyclotron Laboratory was fragmented on a 300 mg/cm² ^9Be target which produced secondary beams. These secondary beams were transported by the A1200 analyzing system [12] to the Si detector telescope. In this system the beams were partially purified by polyethylene wedges, and their energy dispersions were limited to $\leq 1\%$ FWHM by analyzing slits. For example, one A1200 setting delivered usable quantities of ^{11}C , ^{12}N , and ^{13}O at energies of 41, 46, and 51 MeV/nucleon, respectively.

The Si target-detector telescope is shown schematically as an inset to Figure 1. The first two detectors, which we call D1 and D2, were position-sensitive detectors (PSD's), with thickness 0.2 mm, lateral dimensions 2.5 cm x 2.5 cm, and 60 cm separation. They measured projectile coordinates normal to the beam axis, defining beam of 5 mm radius. Energy losses in these detectors identified the desired projectiles, but allowed some contaminants as we discuss later. The next five detectors, called D3 through D7, were about 0.5 mm thick and had active areas from 300 to 600 mm². They stopped all non-

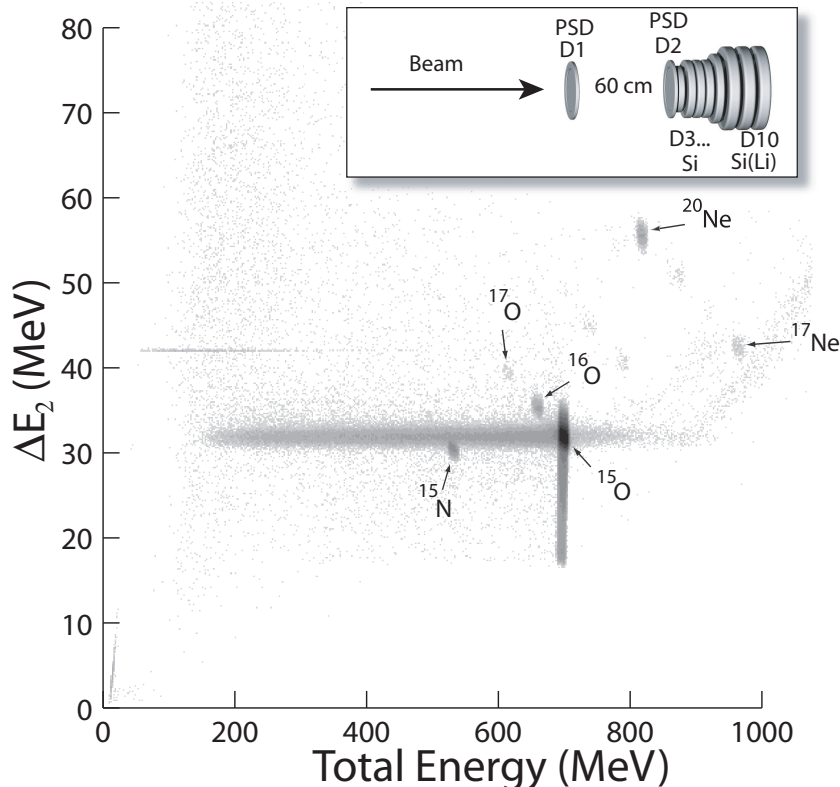


FIG. 1: (color online) Scatter plot of ΔE_2 vs. total energy deposited in the telescope, for incident 48 MeV/nucleon ^{15}O . Most contaminants ($^{16,17}\text{O}$, ^{17}Ne , etc.) are removed by gating on ΔE_2 ; the treatment of ^{15}N is described in the text. The inset shows the target-detector telescope used for measurements.

reacting projectiles with $A \geq 11$ and served as targets for reactions, including breakup. The final Li-drifted detector, D8, had 5 mm thickness and about 4 cm diameter. It stopped projectiles with $A \leq 10$ and the longer-ranged breakup fragments. All detectors except D1 were close-packed. Detectors D9 and D10 were not used in this experiment, but were utilized in a concurrent measurement of σ_R 's in the Be isotopes [13].

The scatter plot of Fig. 1 illustrates our secondary beam composition. It shows ΔE_2 , the energy deposited in D2, vs. the total energy loss in the telescope, for properly-aimed projectiles tentatively identified as ^{15}O by their energy loss in D1. The non-reacting projectiles are the most dense group, labeled ^{15}O . Events in the horizontal tail to the left react downstream of D2, and the few to the right are either pileup or positive Q-value reactions. Events in the vertical tail are non-reacting projectiles with significant energy straggling in D2.

Several contaminant groups, with magnetic rigidities in the A1200 system identical to that of 48 MeV/nucleon ^{15}O , also are observed in Fig. 1. Most of these, e.g. $^{16,17}\text{O}$ and $^{17,20}\text{Ne}$, are so well resolved that a gate on ΔE_2 removes them completely. The treatment of the remaining ^{15}N contaminant is described in the next section.

III. EVENT SELECTION AND DATA ANALYSIS

A. σ_R Measurements

Spectra of total energy deposited in the Si telescope by incident 48 MeV/nucleon ^{15}O projectiles appear in Fig. 2. Each of these four spectra shows a prominent peak for non-reacting projectiles and, below this peak, a continuum due to reactions.

Events in the spectrum labeled D_{1-2} are from projectiles with acceptable positions and normal ^{15}O energy losses in Detectors D1 and D2. The ^{15}O reactions beneath the ^{15}N contaminant peak are extracted by assuming a linear energy dependence of the ^{15}O reaction yield near that peak. The contribution from small Q-value reactions is included by extrapolating the ^{15}O reaction yield just below the full energy peak to its center. The probability η_2 of a reaction occurring anywhere downstream of Detector D2 then equals the ratio of reactions to total events in this spectrum, which are mainly in the sharp peak. The spectrum labeled D_{1-3} has an additional gate requiring normal ^{15}O ionization in D3, and therefore gives the probability η_3 for a reaction to occur

beyond that detector. Since a non-reacting ^{15}O projectile drops in energy from 44 to 38 MeV/nucleon in Detector D3, the average cross section for this energy range is

$$\sigma_R = (\eta_2 - \eta_3)/N_3 \quad (1)$$

where Detector D3 has N_3 target nuclei per unit area. Similarly, the σ_R 's for the energy ranges 38 to 31 MeV/nucleon and 31 to 22 MeV/nucleon are determined by $(\eta_3 - \eta_4)/N_4$ and $(\eta_4 - \eta_5)/N_5$, respectively. Corrections were made for attenuation of the beam in the individual detectors; these were less than 1% in all cases.

Our σ_R data are presented in Table I. The main experimental uncertainties are statistical in origin: the counts in the reaction region, subtraction of contaminant events, and extrapolation to the non-reacting-projectile peak center in Fig. 2. Events above the peak are believed to be mainly pileup. If treated similarly to those below the peak, they would add about 1.5%, or .02 b, to the σ_R 's quoted in Table I. Given the uncertain origin of these events, we make no correction to σ_R but add 2% uncertainty in quadrature to the experimental uncertainties. A further 2% uncertainty in the detector thicknesses is also included.

The contaminants produced very few reactions which were counted in the reaction continuum. For example, there are about 1700 non-reacting ^{15}N events in the D_{1-2} spectrum of Fig. 2, compared with 3.2×10^6 ^{15}O 's. Hence the reactions by contaminants add about 0.05% to the measured σ_R 's. No correction was made for this effect since it is so small and the contaminants' reaction cross sections are not well known.

B. σ_p Measurements

The heavy fragments from proton removal generally have longer ranges than the projectiles which produce them. For example, all projectiles with $A \geq 11$ stopped in Detector D7, but most produced some fragments which stopped in D8 along with others which stopped in D7. The exception was ^{13}O which had detectable yield only for ^{12}N stopping in D7. Projectiles with $A \leq 10$, and all of their fragments, stopped in D8. Particle identification (PID) was used to select fragments of interest. The PID parameter for fragments stopping in Detector 7 is obtained from the energy losses ΔE_6 and ΔE_7 , through the equation

$$PID = A[(\Delta E_6 + \Delta E_7)^p - (\Delta E_7)^p], \quad (2)$$

where $p = 1.73$ and the arbitrary constant A is chosen to place the peaks of interest in convenient channels. A similar equation, relating energy losses ΔE_7 and ΔE_8 , identifies those fragments stopping in D8.

Fragment identification was basically restricted to those produced in Detectors D3 through D5. A tight ΔE_2 gate limited the production region in D2 to about

its last 0.03 mm, which increased the effective production target thickness. Fragments produced earlier in D2 were rejected because of their decreased ionization. Production in D6 and beyond was excluded by counting only events with significantly lower ΔE_5 than that of non-reacting projectiles. This rejected some events produced in D5 near its rear face, and we made a model correction for this loss.

As an example, we discuss the boron isotopes produced by incident 37 MeV/nucleon ^{11}C . A PID spectrum for fragments stopping in D7 appears in Fig. 3. The dominant isotope produced is ^{10}B , with lesser amounts of ^{11}B (through charge exchange) and ^8B (via some more complex process). The gap between the ^8B and ^{10}B groups reflects the absence of ^9B , which is unbound.

Several corrections were made to the observed fragment yields. The largest of these was for rejection of fragments produced in D5, near its rear face, by the software gate on ΔE_5 mentioned earlier. This correction required the fragment momentum distribution in the kinematic center of mass system (c.m) of the incident projectile, which was calculated from Goldhaber's [7, 14] theory. Typically, 10% of the fragments stopping in D7, but none of those stopping in D8, were rejected. No fragments produced before D5 were rejected by this gate; thus, the overall event loss it caused was typically 3%. Since fragment production in D2 increased the effective target thickness by about 2%, the observed yield was reduced by this amount. The loss of projectiles by reactions in D3 through D5, added to that of produced fragments lost to secondary reactions and hence misidentified, was about 1%. Possible corrections for fragments transmitted through D8 or stopping short of D7 were found to be negligible.

The beam contaminants mentioned earlier had no effect on these measurements due to their short range. For example, the 37 MeV/nucleon ^{15}N contaminant in the 48 MeV/nucleon ^{15}O beam (see Figs. 1 and 2) stops in Detector D6. In contrast, the ^{14}N fragments produced from ^{15}O breakup reached at least D7.

The ratio of the combined corrected fragment yield to the incident flux (projectiles with acceptable positions and energy losses in D1 and D2) gave the breakup cross section; these are presented in Table II. The uncertainties listed therein were found by adding in quadrature the statistical uncertainties and an uncertainty of 1/3 of the combined corrections to the data.

IV. THEORETICAL PREDICTIONS, AND COMPARISON WITH MEASUREMENTS

A. Reaction cross sections

Experimental reaction cross section data are shown in Fig. 4. We first compare these data with the predictions of the strong absorption model of Kox [15]. In this model

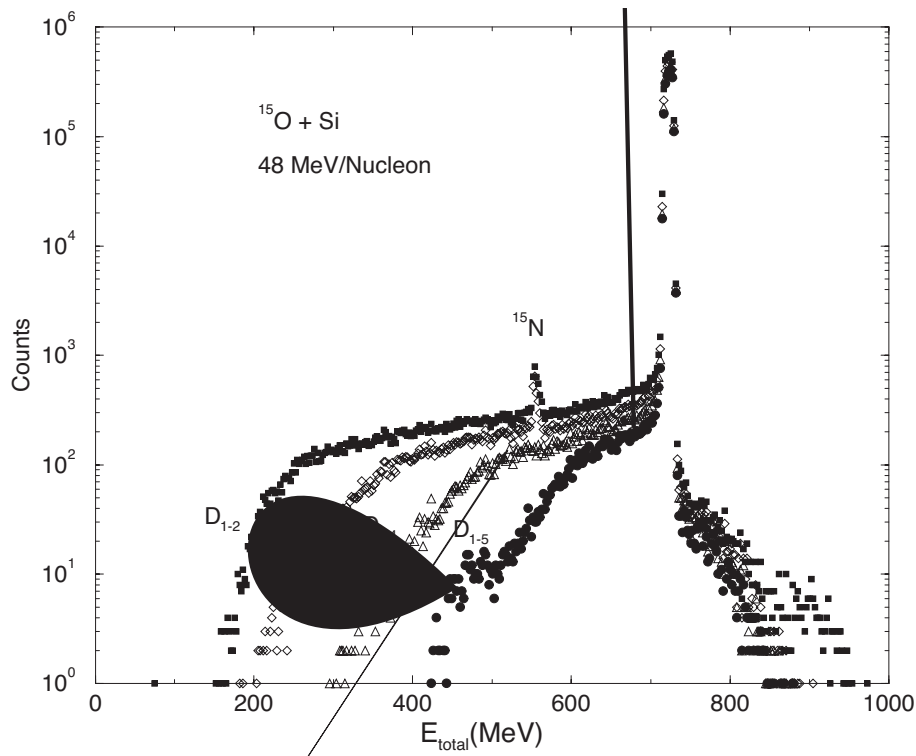


FIG. 2: Total energy spectra of 48 MeV/nucleon ^{15}O incident upon the Si telescope, gated to exclude events which react before detectors D3, D4, D5, or D6. The difference in reaction probabilities between curves labeled D_{1-2} and D_{1-3} determines σ_R at the energies the incident projectiles have in D3, after ^{15}N contaminant events are subtracted.

the reaction cross section is

$$\sigma_R(E) = \pi r_0^2 \left(A_p^{1/3} + A_t^{1/3} + a \frac{A_p^{1/3} A_t^{1/3}}{A_p^{1/3} + A_t^{1/3}} - C(E) \right)^2 \times \left(1 - \frac{V_c}{E_{c.m.}} \right) \quad (3)$$

where $A_{p(t)}$ are the projectile (target) mass numbers, $a = 1.85$ is a mass symmetry parameter related to the volume overlap of projectile and target, and $C(E)$ is a correction related to the transparency of the optical potential. We adopt here the linear approximation of Mittig *et al.*[16], $C(E) = 0.31 + 0.0147E/A$ which gives reasonable results for the range of energies studied here. Bending of trajectories in the target Coulomb field is taken into account by the last factor in Eq. 3. There, the Coulomb potential is evaluated at $R_c = \left[1.07 \left(A_p^{1/3} + A_t^{1/3} \right) + 2.72 \right]$ fm.

The Kox formula gives excellent results for stable nuclei when the reduced strong absorption radius is fixed at $r_0 = 1.1$ fm, and therefore any significant departure from its predictions may disclose a halo structure. The calculations shown in Fig. 4 were done using the standard value for r_0 , except for ^6Li and ^9C where a somewhat larger value ($r_0 = 1.15$ fm) was needed to fit the data. This variation must relate to the weak binding of the last two nucleons in each of these nuclei. It should be noted that the variation $\Delta r_0 = 0.05$ fm adds 130 mb to σ_R for ^6Li at

30 MeV/nucleon.

In Figure 5 we display the A -dependence of the Kox σ_R predictions, using $r_0 = 1.10$ fm for all projectiles, at an energy of 35 MeV/nucleon. To compare them with our measurements, predictions for all projectiles were individually renormalized to best fit the energy dependence of each projectile's σ_R data. The renormalized calculations at 35 MeV/nucleon are plotted as interpolated “data” in Figure 5. The smooth A dependence of the predictions reproduces the data on average, but is unable to explain the scatter of the reaction cross sections observed in the experiment. This observation suggests that a more sophisticated theory is needed to explain these data.

We next use the optical limit (OL) of the Glauber multiple scattering theory. The reaction cross section is given by

$$\sigma_R = 2\pi \int_0^\infty b[1 - T(b)]db, \quad (4)$$

where b is the impact parameter, and the transparency function (or elastic survival probability) $T(b)$ is given by

$$T(b) = \exp[-\chi(b)]. \quad (5)$$

The quantity $[1 - T(b)]$ is called the opacity or nuclear

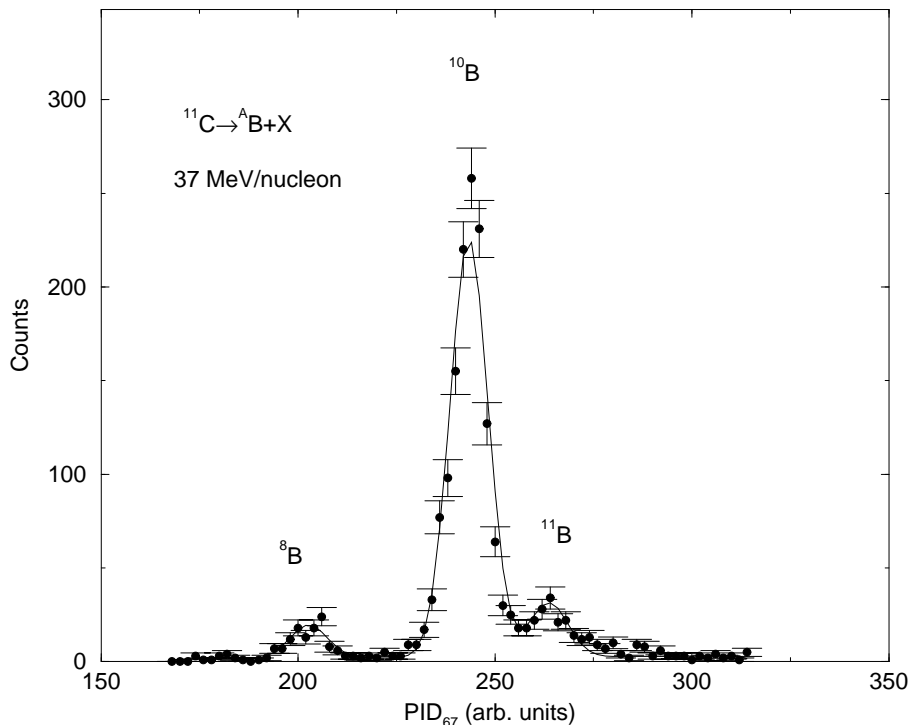


FIG. 3: Particle identification spectra for bound B isotopes produced in Detectors D3 through D5 and identified in D6 and D7, with 41 MeV/nucleon ^{11}C incident upon the telescope. Note the absence of a group due to ^9B , which is unbound.

shadow. The scattering phase is given by

$$\chi(b) = \sum_{\alpha,\beta=p,n} \sigma_{\alpha\beta}^{NN}(E) \int d\vec{b}_1 d\vec{b}_2 \tilde{\rho}_\alpha(b_1) \tilde{\rho}_\beta(b_2) \delta(\vec{b}_1 + \vec{b}_2 - \vec{b}) \quad (6)$$

where the sum runs over all NN isospin channels. Here we assume a zero-range nuclear force and charge symmetry for the free NN cross sections ($\sigma_{pp} = \sigma_{nn}$). These are taken from the parametrization of John *et al.*[17]. We ignore in-medium effects, Pauli blocking, and Fermi motion, and assume a purely imaginary forward NN scattering amplitude. In principle, one should correct Eq. 4 for Coulomb dissociation effects. Estimation of this mechanism (see next subsection) leads to the conclusion that its contributions are negligibly small. They amount to 2 mb for ^7Be and 20 mb for ^{12}N Coulomb breakup at 35 MeV/nucleon, well within the experimental uncertainties. The profile functions $\tilde{\rho}$ needed in Eq. 6 are calculated by Abel transformation of the ordinary particle densities ρ in coordinate space,

$$\tilde{\rho}(b) = \int_{-\infty}^{+\infty} \rho(\sqrt{b^2 + z^2}) dz \quad (7)$$

Correction for bending of the trajectories in the target Coulomb field is introduced as follows. Eq. 4 is rewritten as

$$\sigma_R = 2\pi \int_0^\infty b[1 - T(b')] db \quad (8)$$

where $b' = (1/k) \left(\eta + \sqrt{\eta^2 + k^2 b^2} \right)$ is the impact parameter for a grazing Coulomb trajectory, η is the Sommerfeld parameter, and k the wave number. After some algebra one obtains

$$b^2 = b'^2 \left(1 - \frac{V_c(b')}{E_{c.m.}} \right). \quad (9)$$

Using $V_c(b') \approx V_c(R_c)$ with R_c defined above, one obtains

$$\sigma_R = 2\pi \left(1 - \frac{V_c(R_c)}{E_{c.m.}} \right) \int_0^\infty b'[1 - T(b')] db' \quad (10)$$

which also justifies the correction made in Eq. (3).

The single particle densities used in this analysis were obtained from a standard spherical HF+BCS calculation using the density functional of Beiner and Lombard [18]. The surface strength of the functional has been slightly adjusted to reproduce the known experimental binding energies. The *rms* radii from HF calculations are listed in Table III. They show a surprisingly good agreement with experimental data from high energy reactions [19] and those obtained from the present σ_R data, as described below, especially for the loosely bound nuclei ^7Be , ^9C , ^{12}N , ^{13}O and ^{17}Ne . The results with the OL model are displayed in Figs. 4 and 5. Clearly, the mass dependence of the reaction cross section is well reproduced since this approximation incorporates realistic densities.

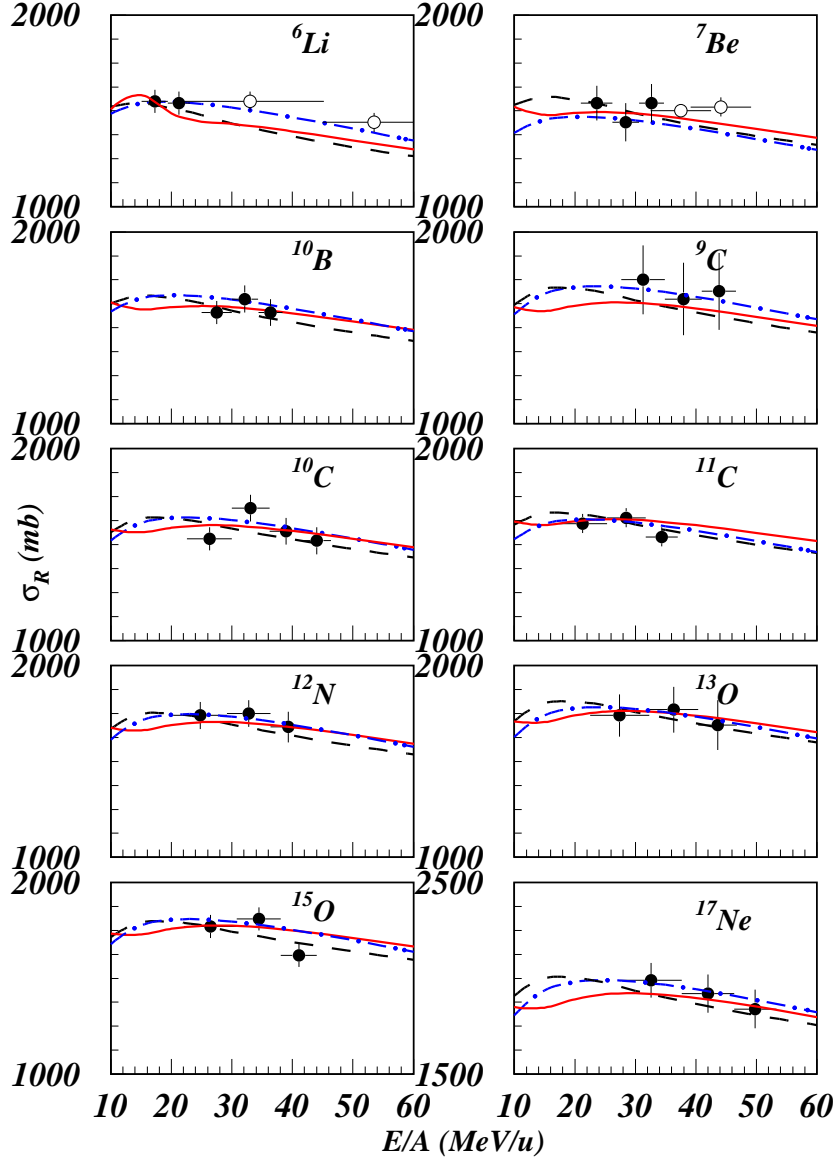


FIG. 4: (color online) Experimental reaction cross sections (filled points) compared with predictions from the Kox phenomenological formula (dash-dotted lines), the optical limit of the Glauber model (dashed lines) and the JLM microscopic folding model (continuous lines). Open symbols are data from our earlier work [11, 13]. See text for details.

In the remainder of this section we discuss the ability of the JLM folding model [20] to describe reaction cross sections as a further check of our densities. We adopt their nuclear matter approach which incorporates a complex, energy- and density-dependent parametrization of the effective interaction obtained in the Brueckner Hartree-Fock approximation from the Reid hard-core NN potential. Studies of elastic scattering of p -shell nuclei [21, 22] indicate that the absorptive component of the JLM potential is realistic for loosely bound nuclei and

needs no renormalization ($N_w \approx 1$, see below), while the real part needs a significant renormalization. Here we extend these studies much closer to the proton drip line.

In the JLM model the complex form factor for the optical potential is given by

$$U(R) = \int d\vec{r}_p d\vec{r}_t \rho_p(r_p) \rho_t(r_t) v(\rho, E, s) \quad (11)$$

where v is the (complex) NN interaction, $\rho_{p(t)}$ are the single particle densities of the interacting partners, $\vec{s} =$

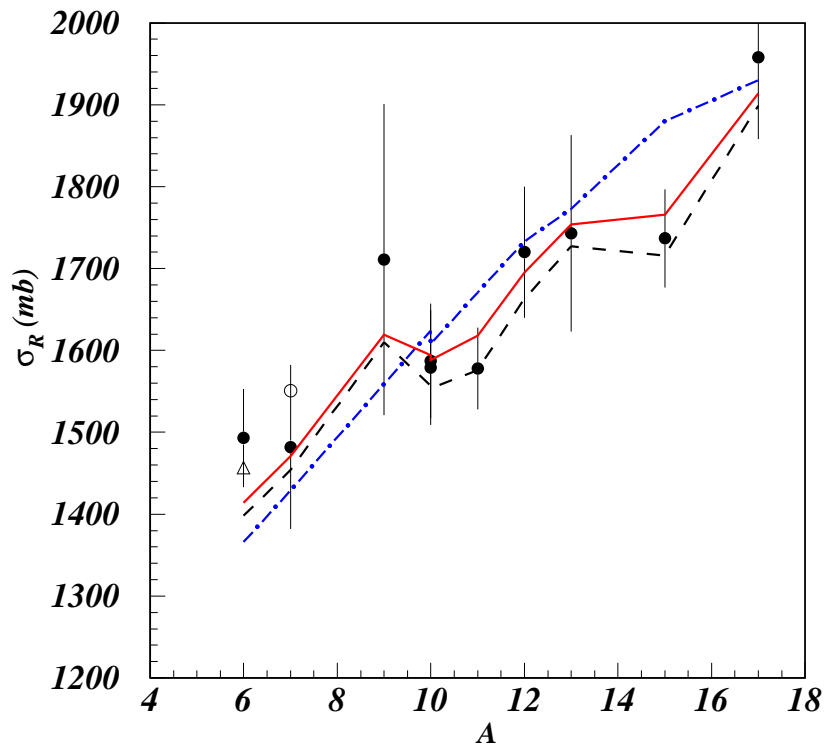


FIG. 5: (color online) Interpolated reaction cross sections at 35 MeV/nucleon (points) as a function of projectile mass number. Theoretical predictions use the Kox model with the standard reduced strong absorption radius $r_0=1.1$ fm (dash-dotted line), Glauber (OL) model (dashed line) and JLM model (full line). Open symbols are optical model values from elastic scattering of ${}^6\text{Li}+{}^{28}\text{Si}$ at 318 MeV (triangle, [24]) and from ${}^7\text{Li}+{}^{28}\text{Si}$ at 350 MeV (circle, [25]).

$\vec{r}_p + \vec{R} - \vec{r}_t$ is the NN separation distance between interacting nucleons and ρ is the overlap density. The effective NN interaction contains an isovector component, which gives a negligibly small contribution for p -shell nuclei. However, it is included here for convenience in conjunction with appropriate single particle isovector densities. The coupling of the entrance channel to the breakup and particle transfer reactions has been described by a dynamic polarization potential (DPP) which is strong and has complicated dependence on radius, mass, and energy [23]. To simulate the radial dependence of a DPP, and to increase the flexibility of the folding potential we introduce a smearing function $h(r)$ to obtain our final folding potential,

$$\tilde{U}(R) = \int d\vec{R}' U(R') h(|\vec{R} - \vec{R}'|) \quad (12)$$

The smearing function $h(r)$ is taken as a normalized Gaussian [20, 22],

$$h(r) = \frac{1}{t^3 \pi^{3/2}} \exp(-r^2/t^2) \quad (13)$$

which behaves as a δ -function for $t \rightarrow 0$, while for finite t values it modifies the *rms* radius of the folding form factor by $r_h^2 = (3/2)t^2$, leaving the volume integral unchanged. It turns out that the smearing procedure described above is essential in simulating the complicated radial dependence of the dynamic polarization potential [21]. To be consistent with the JLM model we take the overlap density in Eq. 11 to be given by

$$\rho = \left[\rho_p(\vec{r}_p + \frac{1}{2}\vec{s}) \rho_t(\vec{r}_t - \frac{1}{2}\vec{s}) \right]^{1/2} \quad (14)$$

This approximation is physically reasonable since the overlap density approaches zero when one of the interacting nucleons is far from the core, and approaches the nuclear matter saturation value for complete overlap. We recall that the JLM model was developed to describe the optical potential for a nucleon traversing nuclear matter, and its density dependence is defined for densities not exceeding the saturation value in nuclear matter.

The model contains four parameters: two normalization constants N_v, N_w and two range parameters t_v, t_w .

They have been fixed here close to standard values for p -shell nuclei [21, 22]: $N_v=0.4$, $N_w=0.85$ and $t_v = t_w = 1.2$ fm. We assume that the energy dependence is weak, and use this set of parameters at all energies and for all projectiles. We are merely interested in a general assessment of the JLM model rather than fitting a particular cross section. The results of this approach are shown with continuous lines in Figs. 4 and 5. Fig. 5 also includes the optical model cross sections obtained by fitting known elastic scattering distributions [24, 25]. One observes an even better description of the scatter effect in the reaction cross sections.

B. Nuclear radii

It is interesting to use reaction cross section data to infer nuclear sizes. At the energies of our experiment, the total NN reaction cross section is large, the mean free path is small, and therefore the heavy ion reaction cross section is strongly influenced by NN collisions at the surface. We chose to describe the tails of the nuclear matter densities by a Gaussian[26]:

$$\rho_i(r) = \rho_{i0} \exp(-r^2/a_i^2), \quad i = p, t, \quad (15)$$

with the normalization,

$$\rho_{i0} = \frac{A_i}{(\sqrt{\pi}a_i)^3}. \quad (16)$$

The slope parameter a_i is related to the nuclear size by

$$\langle r_i^2 \rangle = \frac{3}{2}a_i^2. \quad (17)$$

We let $a^2 = a_p^2 + a_t^2$ and

$$\chi_0 = \overline{\sigma_{NN}}\pi^2\rho_{p0}\rho_{t0}\frac{a_p^3a_t^3}{a^2}, \quad (18)$$

where $\overline{\sigma_{NN}}$ is the isospin-averaged NN cross section. Under these assumptions, Eq. (4) can be solved analytically,

$$\sigma_R = \pi a^2 (C + \ln \chi_0 + E_1(\chi_0)) \left(1 - \frac{V_b}{E_{c.m.}}\right) \quad (19)$$

where $C = 0.5772$ is the Euler constant and E_1 is the exponential integral. Eq. (19) shows essentially the geometric character of the reaction cross section since the leading term is $\sigma_R \approx \pi(r_p^2 + r_t^2)$. The leading term in the Kox formula is $\sigma_R \approx \pi(r_p + r_t)^2$. The energy dependence is governed entirely by σ_{NN} . To extract nuclear sizes from experimental data, we use Eq.(19), with the target rms radius fixed to $r_t=3.05$ fm which we obtained from HF calculations. The compilation of Angeli [27] for rms charge radii indicates a value of $r_{ch}=3.12$ fm for ^{28}Si . We calculate an upper limit of 2% uncertainty from this difference in our theoretical estimations. In practice, the parameter a_p is gridded in small steps until the calculated

cross section equals the experimental value. The results are listed in Table III and displayed in Fig. 6. These values are consistent with those extracted from high energy data within their uncertainties. The values and uncertainties quoted in the table include the weighted averages over various energies measured here, and statistical uncertainties. No provision has been taken to correct values in Table III for nucleon finite size. Assuming a nucleon rms value of $r_n^2 \approx 0.8$ fm², this would increase values in Table III by $\approx 5\%$.

The sensitivity of the cross section to the functional form of the single-particle density is studied using harmonic oscillator wave functions appropriate for the pd -shell nuclei with s and d state admixtures.

$$\rho_\tau(r) = \frac{1}{(\sqrt{\pi}b_\tau)^3} \left(n_s + \frac{2}{3}n_px^2 + \frac{4}{15}n_dx^4 \right) \exp(-x^2) \quad (20)$$

where n_s , n_p and n_d are occupation numbers in the s , p and d shells, b_τ is the range parameter and $x = r/b_\tau$. The finite range of the nuclear force is included in Eq. (6) by replacing the δ force by a finite range NN interaction

$$v(\vec{b}) = \frac{1}{\pi\mu^2} \exp(-b^2/\mu^2) \quad (21)$$

with the interaction range $\mu=1$ fm [28]. The normalization in Eq. (21) ensures that the reaction volume overlap in Eq. 6 is not changed, but the smearing enhances the weight of the density tail and reduces the contribution from the central part of the density. In addition, the number of NN inelastic scatterings in the overlap volume is weighted differently by $\sigma_{pp} \neq \sigma_{np}$. As a result, the rms radii extracted with this method (shown in Table III) are slightly smaller than with the Karol model. Woods-Saxon (WS) shapes are more appropriate for testing the role played by long tails in the projectile neutron and/or proton densities

$$\rho_\tau(r) = \rho_{0\tau} / \left[1 + \exp\left(\frac{r - R_\tau}{a_\tau}\right) \right], \quad \tau = p, n \quad (22)$$

where the $\rho_{0\tau}$ are normalization constants. Equations (4-7) have been solved numerically. The half-radius parameter R_τ is the most sensitive in extracting the nuclear rms radius. No anomalies were found in proton or neutron surface thickness when using $a_p \approx a_n \approx 0.5$ fm for most nuclei, and slightly larger values for ^9C , ^{12}N and ^{17}Ne . The uncertainties shown in Table III are evaluated with the bootstrap method of Efron [29], which has the merit of weakening the influence of systematic errors in the data, and leads to meaningful ranges in the extracted parameters. All these calculations lead to mutually consistent rms radii for the nuclei studied here (Table III).

C. One-proton removal

We use the core spectator model and Glauber multiple scattering theory to calculate one-proton breakup cross

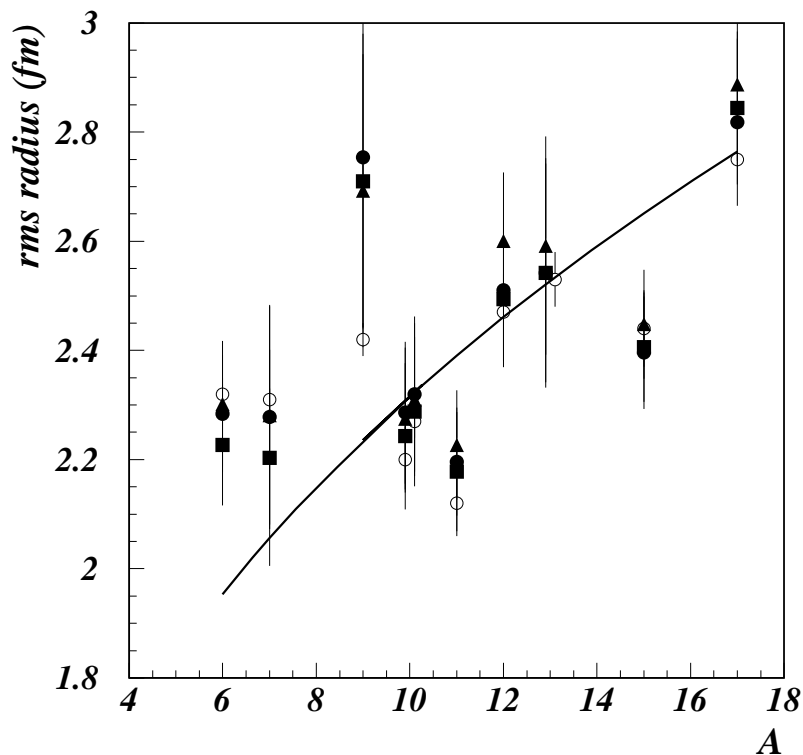


FIG. 6: *rms* radii extracted from reaction cross sections measured in this experiment (filled symbols) using the gaussian density (filled circles), harmonic oscillator density (squares) and Woods-Saxon density (triangles) compared with the values extracted from high-energy interaction cross section [19] (open circles). The line shown is $1.075A^{1/3}$ fm to guide the eye. Error bars are 1σ deviation arising from energy dependence and statistics.

sections. This model has been tested extensively on a number of one-neutron removal reactions of neutron-rich nuclei in the *psd* shell [30]. We approximate the ground state of the projectile (J^π) by a superposition of configurations of the form $[I_c^\pi \otimes nlj]^{J^\pi}$, where I_c denotes the core states and nlj are the quantum numbers specifying the single particle wave function of the outermost proton. The s.p. wave functions were obtained for a Woods-Saxon potential using the effective separation energy recipe $S_p^{eff} = S_p + E_{ex}^c$, where E_{ex}^c is the excitation energy of the core state. The depth of the potential was varied in such a way that the known one-proton separation energy was reproduced. The radius of the WS potential was fixed to values close to the *rms* radius of the core (Table III) and the diffuseness was fixed to $a = 0.5$ fm for all cases.

Fine tuning of these parameters could significantly improve the theoretical results since they determine the asymptotic normalization coefficient of the outermost proton. We neglect dynamical excitation of core states in the reaction. In this approximation, the reaction can

populate core states only to the extent that there is a nonzero spectroscopic factor $C^2S(I_c, nlj)$ in the projectile ground state. The various configurations are assumed to contribute incoherently to the total breakup cross section for a given core state,

$$\sigma_p(I_c^\pi) = \sum_{nlj} C^2S(I_c^\pi, nlj) \sigma_{sp}(nlj, S_p^{eff}). \quad (23)$$

The total breakup cross section (σ_p) is then the sum over all particle-bound states of the core. In the present experiment, the core states were not identified and the removed proton was not detected. Therefore, the dynamical factor σ_{sp} in Eq.(23) includes contributions from stripping, nuclear dissociation and Coulomb dissociation. Other more violent channels, such as core breakup, have been ignored. The nuclear mechanisms have been described using transition operators defined in terms of scattering functions (S-matrix) for p-target and core-target interactions generated in the JLM folding model as described above. Scattering functions in impact parameter representation have been calculated in the eikonal approxima-

tion, including noneikonal corrections up to second order. Coulomb dissociation has been calculated in the first order of perturbation theory. Both $E1$ and $E2$ amplitudes have been included. The interference of these amplitudes does not contribute to the inclusive removal cross section.

The spectroscopic factors $C^2S(I_c, nlj)$ employed here were calculated with the shell model code OXBASH [31] using the WBP [32] interaction within a $1s - 1p - 2s1d - 1f2p$ model space. Excitations up to $4\hbar\omega$ have been included in this single particle model space for most of the cases. Inclusion of higher $n\hbar\omega$ excitations with this effective interaction was shown to better describe some experimental observables [33]. Spurious center-of-mass components of the projectile have been suppressed by the usual method [34] of adding a center-of-mass hamiltonian to the nuclear interaction. In all cases, the experimentally established spin-parity and core excitation energies have been used. The shell model spectroscopic factors have been multiplied by the center-of-mass correction factor $A_p/(A_p - 1)$, following Refs. [35, 36].

The projectile ground state spin-parity (J^π), core spin-parity and excitation energies (E_{ex} , I_c^π), the stripping, diffractive dissociation and Coulomb dissociation cross section, as well as the shell model spectroscopic factors are listed in Table IV. The total inclusive cross section $\sigma_p^{Glauber}$ was corrected for center-of-mass effects as explained above. All calculations were done at 35 MeV/nucleon.

Comparison with experimental values in Table II shows reasonable agreement. It should be noted that the extended Glauber model is designed to describe one nucleon removal reactions for loosely bound nuclei. The wave function of the outermost nucleon is assumed to penetrate substantially into the classically forbidden region, since most of the reaction probability is localized at the surface. The interaction should be strongly absorptive. In addition, the core is assumed to be compact and well decoupled from the outermost nucleon. A special case is ^{10}B which has a quite large one-proton separation energy ($S_p \approx 6.8$ MeV), and a relatively fragile core, ^9Be . In this case the reaction is not completely peripheral, with significant contributions arising from impact parameters $b \leq R_c$, where R_c is the core radius. The calculated breakup cross section exceeds the experimental value by more than 50%. Only by excluding contributions from the nuclear interior can one obtain a reasonable value (Table IV).

D. Discussion of Results

The reaction cross sections for ^6Li measured in this experiment and at higher energy [11] show in Fig. 4 a smooth energy dependence, falling at 50 MeV/nucleon, which is well fitted by the Kox model and slightly underpredicted by the Glauber models. For ^7Be we see a flat energy dependence, with all models slightly underpredicting the 40 MeV/nucleon datum.

Figures 4 and 5 show a large reaction cross section for the ^9C projectile. Both Glauber (OL) and JLM models predict this increase, in reasonable agreement with the experiment. The *rms* radius obtained from our present data exceeds by about 12% the value obtained from high energy data [19], and it is close to that obtained for ^{17}Ne , another loosely bound nucleus. The smaller Coulomb barrier in ^9C enhances the penetrability of the outermost proton much beyond the range of nuclear forces and this compensates the larger interaction volume provided by ^{17}Ne . Unfortunately, the uncertainty is relatively large and the halo structure of this nucleus cannot be firmly established. More accurate experimental data are needed to clarify this point.

The reaction cross sections for ^{10}B , ^{10}C , and ^{11}C are definitely smaller than for ^9C and not much larger than those of ^6Li and ^7Be . The extracted *rms* radius of ^{11}C is quite small though in agreement with high energy data [19]. An independent measurement by Liatard *et al.*[37] indicates a much larger value, 2.46 ± 0.30 fm, in agreement with our HF calculation of 2.48 fm (see Table III). ^{12}N seems to behave normally. Both Glauber (OL) and JLM models give an excellent description of the cross section. The extracted radii seem to be in good agreement with HF calculations (see Table III).

Figure 5 shows that σ_R stays nearly constant from ^{12}N through ^{15}O , as predicted by the JLM and OL (but not the Kox) models. For well-bound projectiles we expect an increase with increasing A . However, S_p is 0.6, 1.5 and 7.3 MeV for ^{12}N , ^{13}O and ^{15}O , respectively, and the weaker binding of the two lighter nuclei increases the range of their valence protons. The two effects appear to roughly compensate for each other.

Among the nuclei we studied, ^{12}N has by far the largest one proton removal reaction cross section. Furthermore, the p -removal process for this case is related to $^{11}\text{C}+p$ radiative capture. Depending on their initial CNO abundances, this reaction may have been important in some super-massive stars in the early universe, allowing the stars to explode as supernovae rather than collapsing as black holes before ejecting any mass.[38, 39]. The asymptotic normalization coefficient (ANC) for $^{12}\text{N} \rightarrow ^{11}\text{C}+p$ has been measured recently using transfer reactions [40]. However, these reaction-rate data are ambiguous and therefore it is desirable to remeasure the ANC by breakup, as an independent check. The one proton separation energy is small ($S_p = 0.6$ MeV), and thus ^{12}N could be a proton halo candidate. The Glauber model nicely reproduces the measured σ_p . However, the shell model calculations suggest a very fragmented structure for the g.s. wave function, significant contributions arising from (g.s, $3/2^- \otimes 1p_{1/2}$), (g.s, $3/2^- \otimes 1p_{3/2}$) ($E_x=2.0$ MeV, $1/2^- \otimes 1p_{3/2}$) and ($E_x=4.8$ MeV, $3/2^- \otimes 1p_{1/2}$). The ANC's have been measured [40], for the core ground state components; they are $C_{1p_{1/2}}^2 = 1.4 \pm 0.2 \text{ fm}^{-1}$ and $C_{1p_{3/2}}^2 = 0.33 \pm 0.05 \text{ fm}^{-1}$. Since the single particle normalization coefficients are almost identical for the $1p_{1/2}$ and $1p_{3/2}$ wave functions, one should have approxima-

tively $S_{1p_{1/2}}/S_{1p_{3/2}} \approx C_{1p_{1/2}}^2/C_{1p_{3/2}}^2$, a relation that is satisfied for the states mentioned above for which the experimental values of the ANC are known, when one uses the corresponding shell model spectroscopic factors listed in Table IV. The reaction cross section measurements showed no anomaly for this nucleus. The calculated parallel and transverse core fragment momentum distributions are narrow ($\text{FWHM}_z \sim 86 \text{ MeV}/c$, $\text{FWHM}_x \sim 120 \text{ MeV}/c$) comparable to that found for a well established halo nucleus, such as ^8B [4]. The halo character of ^{12}N could not be firmly established on the basis of the present data. More precise reaction and breakup cross section data are needed as well as a clear separation of contributions from core excited states.

For halo nuclei, one can assume that the core is decoupled from the halo nucleon, and the following decomposition of the absorption operator (Eq. 4) holds

$$1 - T \approx 1 - T_c T_h = (1 - T_c) + T_c(1 - T_h) \quad (24)$$

Here, the first bracketed term on the right describes the core absorption (in the absence of the halo particle), while the second describes the absorption of the halo particle, weighted by the core survival probability. One can associate this last term with the stripping component of the total breakup cross section σ_p . Assuming that the diffractive dissociation and Coulomb dissociation components are small, one can approximate $\sigma_R = \sigma_R^c + \sigma_p$. The difference of the σ_R 's given for ^{11}C and ^{12}N in the middle energy bins of Table I (at energies 28 and 33 MeV/nucleon, respectively) is $110 \pm 86 \text{ mb}$. This agrees with the breakup cross section of $120 \pm 6 \text{ mb}$ given in Table II, though with a large uncertainty.

^{15}O has a one-proton separation energy S_p four times larger than ^{13}O , yet the ^{15}O breakup cross section is two times larger. We expect a larger S_p to give a smaller σ_p and so the Glauber model, which is very sensitive to the separation energy, is not able to reproduce this behaviour. This anomaly probably results from competition with $2p$ -breakup; we found that the ^{13}O breakup produces more C than ^{12}N , though the C yield is isotopically unresolved. Other similar cases were observed for nuclei which have one nucleon outside a fragile core. For example, ^{12}Be , which has one neutron loosely bound to a neutron halo nucleus ^{11}Be , has a smaller σ_n than σ_{2n} [13]. ^9C behaves similarly for proton removal [7].

V. CONCLUSIONS

We have measured reaction cross sections σ_R and one-proton removal cross sections σ_p for a range of stable and short-lived nuclei close to the proton drip line. These σ_R extend our earlier measurements to projectiles of higher A and Z. Comparison with earlier, higher energy data for ^6Li and ^7Be shows a reasonable energy dependence. The optical limit of the multiple scattering Glauber model, and double folding optical potentials derived from the NN effective interaction in nuclear matter, are about

equally successful in describing the data, including their energy- and mass-dependence. However, more accurate data would be needed to distinguish between them or to test sensitively for nuclei with weak halos.

Root-mean-square nuclear radii have been extracted using Glauber theory and three different functional forms for the projectile single particle densities. These results are mutually consistent and in good agreement with values extracted from high energy data, except for ^9C in which case a significantly larger radius has been found.

One proton removal cross sections vary widely. These reactions were described within an extended Glauber model by incorporating fundamental NN interactions and spectroscopic factors from the shell model. The large σ_p in the ^{12}N case suggests a possible weak halo, although the wave function is fragmented into many components. An anomaly has been found in the A=12-15 region, where the one-proton removal cross sections and total reaction cross sections do not behave as expected from proton separation-energy systematics. More experimental and theoretical effort should be devoted to a better understanding of the competition between $-1p$ and $-2p$ channels for nuclei, such as ^{13}O , where the last proton's separation energy exceeds that of the next one (i.e., $S_p > \frac{1}{2}S_{2p}$).

VI. ACKNOWLEDGMENTS

We benefitted from useful discussions with Shalom Shlomo. We thank J. J. Kruse, M. Y. Lee, T. W. O'Donnell, P. Schwandt, H. Thirumurthy, J. Wang, J. Woodroffe, and J. A. Zimmerman for assistance with these measurements. One of us (F.C.) acknowledges support by the Texas A&M University Cyclotron Institute. Additional support from the following National Science Foundation grants PHY-9971836 (UM-Dearborn), PHY02-44989 (Notre Dame and UM-Ann Arbor), PHY0244453 (Central Michigan University) is acknowledged. B. Davids also acknowledges additional support from the Natural Sciences and Engineering Research Council of Canada.

-
- [1] Pftzner, M. *et al.*, Euro. Phys. J. **A 14**, 279-285 (2002)
- [2] J. Giovinazzo *et al.*, Phys. Rev. Lett. **89**, 102501 (2002).
- [3] R.E. Warner *et al.*, Phys. Rev. **C52**, 1166(R) (1995).
- [4] J. H. Kelley *et al.*, Phys. Rev. Lett **77**, 5020 (1996).
- [5] M. H. Smederg *et al.*, Phys. Lett. **B 452**,1 (1999).
- [6] B. Davids, S.M. Austin, D. Bazin, H. Esbensen B.M. Sherrill, I.J. Thompson, and J.A. Tostevin, Phys. Rev. **C63**, 065806 (2001).
- [7] R.E. Warner, F.D. Becchetti, J.A. Brown, A. Galonsky, J. H. Kelley, A. Nadasen, R.M. Ronningen, J.A. Tostevin, J.S. Winfield, and P. Zecher, Phys. Rev. **C69**, 024612 (2004).
- [8] R. Kanungo *et al.*, Phys. Lett. **B571**, 21 (2003).
- [9] R. E. Warner *et al.*, Nucl. Phys. **A635**, 292 (1998).
- [10] D.W. Litzenberg, D.A. Roberts, M.Y. Lee, K. Pham, A.M. Vander Molen, R. Ronningen and F.D. Becchetti, Med. Phys. **26**, 992 (1999).
- [11] R. E. Warner *et al.*, Phys. Rev. **C54**, 1700 (1996).
- [12] B. M. Sherrill, D. J. Morrissey, J. A. Nolen, Jr., N. A. Orr, and J. A. Winger, Nucl. Instrum. Methods Phys. Res. **B70**, 298 (1992).
- [13] R. E. Warner *et al.*, Phys. Rev. **C64**,044611 (2001).
- [14] A. S. Goldhaber, Phys. Lett. **B53**, 306 (1974).
- [15] S. Kox *et al.*, Phys. Rev. **C35**, 1678 (1987).
- [16] W. Mittig *et al.*, Phys. Rev. Lett. **59**, 1889 (1987).
- [17] S. John, L. W. Townsend, J. W. Wilson, and R. K. Tripathi, Phys. Rev. **C48**, 766 (1993).
- [18] M. Beiner and R. J. Lombard, Ann. Phys. **86**, 262 (1974).
- [19] A. Ozawa, I. Tanihata, T. Kobayashi, Y. Sugahara, O. Yamakawa, K. Omata, K. Sugimoto, D. Olson, W. Christie, and H. Wieman, Nucl. Phys. **A608**, 63 (1996).
- [20] J. P. Jeukenne, A. Lejeune and C. Mahaux, Phys. Rev. **C16**, 80 (1977).
- [21] F. Carstoiu, L. Trache, R. E. Tribble and C. A. Gagliardi, Phys. Rev. **C70**,054610 (2004).
- [22] L. Trache, A. Azhari, H. L. Clark, C. A. Gagliardi, Y.-W. Lui, A. M. Mukhamedzhanov, R. E. Tribble and F. Carstoiu, Phys. Rev. **C61**, 024612 (2000).
- [23] R. S. Mackintosh and K. Rusek, Phys. Rev. **C67**, 034607 (2003).
- [24] A. Nadasen *et al.*, Phys. Rev. **C47**, 674 (1993).
- [25] A. Nadasen *et al.*, Phys. Rev. **C52**, 1894 (1995).
- [26] P. J. Karol, Phys. Rev. **C11**, 1203 (1975).
- [27] I. Angeli, Heavy Ion Physics **8**, 23 (1998).
- [28] G. F. Bertsch, B. A. Brown and H. Sagawa, Phys. Rev. **C39**, 1154 (1989).
- [29] P. Diaconis and B. Efron, Sci. Am. **248**, 116 (1983).
- [30] E. Sauvan *et al.*, Phys. Rev. **C69**, 044603 (2004).
- [31] B. A. Brown, A. Etchegoyen, W. D. M. Rae, Report MSUCL-524 1988.
- [32] E. K. Warburton and B. A. Brown, Phys. Rev. C **46**, 923 (1992).
- [33] M. Horoi, G. Clausnitzer, B. A. Brown, and E. K. Warburton, Phys. Rev. C **50**, 775 (1994).
- [34] D. H. Gloeckner, and R. D. Lawson, Phys. Lett. **53 B**, 313 (1974).
- [35] A.E.L. Dieperink and T. de Forest, Phys. Rev. **C 10**, 543 (1974).
- [36] B. A. Brown, P. G. Hansen, B. M. Sherrill, J. A. Tostevin, Phys. Rev. **C65**, 061601(R) (2004).
- [37] E. Liatard *et al.*, Europhys. Lett. **13**, 401 (1990).
- [38] G. M. Fuller, S. E. Woosley, and T. A. Weaver, Astrophys. J. **307**, 675 (1986).
- [39] M. Wiescher, L. Buchmann, and F.-K. Thielemann, Astrophys. J. **343**, 352 (1989).
- [40] X. Tang, A. Azhari, C.A. Gagliardi, A.M. Mukhamedzhanov, F. Pirlpesov, L. Trache, R.E. Tribble, V. Burjan, V. Kroha, and F. Carstoiu, Phys. Rev. **C67**, 015804 (2003).

VII. TABLES

TABLE I: Total reaction cross sections, σ_R , for ten light isotopes on Si, averaged between the listed energies.

System	Energy interval (MeV/nucleon)	σ_R (b)
${}^6\text{Li}+\text{Si}$	15.1-19.4	1.55 ± 0.06
	19.4-23.1	1.54 ± 0.06
${}^7\text{Be}+\text{Si}$	21.0-26.2	1.54 ± 0.09
	26.2-30.6	1.44 ± 0.10
	30.6-34.7	1.54 ± 0.10
${}^{10}\text{B}+\text{Si}$	25.0-30.0	1.58 ± 0.06
	30.0-34.3	1.65 ± 0.07
	34.3-38.4	1.58 ± 0.07
${}^9\text{C}+\text{Si}$	27.7-34.9	1.75 ± 0.18
	34.9-41.0	1.65 ± 0.19
	41.0-46.6	1.69 ± 0.20
${}^{10}\text{C}+\text{Si}$	22.6-30.0	1.53 ± 0.06
	30.0-36.2	1.69 ± 0.07
	36.2-41.7	1.57 ± 0.07
	41.7-46.4	1.52 ± 0.07
${}^{11}\text{C}+\text{Si}$	17.3-25.3	1.61 ± 0.05
	25.3-31.7	1.64 ± 0.05
	31.7-37.0	1.54 ± 0.05
${}^{12}\text{N}+\text{Si}$	20.3-29.2	1.74 ± 0.07
	29.2-36.4	1.75 ± 0.07
	36.4-42.2	1.68 ± 0.08
${}^{13}\text{O}+\text{Si}$	22.5-32.3	1.74 ± 0.11
	32.3-40.4	1.77 ± 0.12
	40.4-46.8	1.69 ± 0.13
${}^{15}\text{O}+\text{Si}$	22.1-30.8	1.77 ± 0.06
	30.8-38.1	1.81 ± 0.06
	38.1-44.0	1.62 ± 0.06
${}^{17}\text{Ne}+\text{Si}$	27.5-37.7	1.99 ± 0.09
	37.7-46.3	1.92 ± 0.10
	46.3-53.3	1.84 ± 0.10

TABLE II: Proton-removal cross sections for light nuclei on Si, averaged between the specified energies. The Glauber theoretical predictions are described in Section IV C.

Projectile, cross section	Fragment	Energy interval (MeV/nucleon)	Measurement (mb)	Glauber (mb)
${}^7\text{Be}, \sigma_{1p}$	${}^6\text{Li}$	26-38	90 ± 6	117
${}^{10}\text{B}, \sigma_{1p}$	${}^9\text{Be}$	30-42	41 ± 3	62
${}^{11}\text{C}, \sigma_{1p}$	${}^{10}\text{B}$	17-37	53 ± 2	78
${}^{12}\text{N}, \sigma_{1p}$	${}^{11}\text{C}$	20-42	120 ± 6	130
${}^{13}\text{O}, \sigma_{1p}$	${}^{12}\text{N}$	23-49	31 ± 5	56
${}^{15}\text{O}, \sigma_{1p}$	${}^{14}\text{N}$	22-44	64 ± 3	46
${}^{17}\text{Ne}, \sigma_{2p}$	${}^{15}\text{O}$	28-53	223 ± 18	

TABLE III: Proton (r_π), neutron (r_ν), and matter (r_m) rms radii from HF calculations are given in Columns 2 through 4. Column 5 gives experimental values extracted from high-energy reaction cross sections [19]. The last three columns show experimental values extracted from our present data, using Glauber theory (OL) and assuming gaussian, harmonic oscillator, and Woods-Saxon densities.

Nucleus	r_π	r_ν	r_m	$r_m(\text{exp})$ [19]	$r_m(\text{gauss})$	$r_m(\text{HO})$	$r_m(\text{WS})$
${}^6\text{Li}$	2.33	2.31	2.32	2.32 ± 0.03	2.28 ± 0.10	2.23 ± 0.11	2.30 ± 0.12
${}^7\text{Be}$	2.49	2.24	2.39	2.31 ± 0.02	2.28 ± 0.20	2.20 ± 0.19	2.28 ± 0.20
${}^{10}\text{B}$	2.46	2.46	2.46	2.20 ± 0.06	2.29 ± 0.13	2.24 ± 0.13	2.27 ± 0.13
${}^9\text{C}$	2.76	2.25	2.60	2.42 ± 0.03	2.75 ± 0.34	2.71 ± 0.26	2.69 ± 0.25
${}^{10}\text{C}$	2.57	2.31	2.47	2.27 ± 0.03	2.32 ± 0.14	2.29 ± 0.14	2.31 ± 0.14
${}^{11}\text{C}$	2.53	2.41	2.48	2.12 ± 0.06	2.20 ± 0.10	2.18 ± 0.11	2.23 ± 0.10
${}^{12}\text{N}$	2.70	2.45	2.60	2.47 ± 0.07	2.51 ± 0.13	2.49 ± 0.12	2.60 ± 0.12
${}^{13}\text{O}$	2.81	2.47	2.69	2.53 ± 0.05	2.54 ± 0.21	2.54 ± 0.20	2.59 ± 0.20
${}^{15}\text{O}$	2.69	2.58	2.64	2.44 ± 0.04	2.40 ± 0.10	2.40 ± 0.10	2.45 ± 0.10
${}^{17}\text{Ne}$	2.98	2.61	2.83	2.75 ± 0.07	2.82 ± 0.15	2.84 ± 0.14	2.89 ± 0.14

TABLE IV: Calculated spectroscopic factors (C^2S) and cross sections $\sigma(I_c^\pi)$ to the core excited states (E_{ex}, I_c^π) populated in single proton removal from the projectile (${}^AZ, J^\pi$) by the silicon target. The contribution arising from stripping σ_{abs} , diffractive dissociation (σ_{diff}) and Coulomb dissociation (σ_{coul}) are detailed. The total inclusive cross section $\sigma_p^{Glauber}$ is corrected for center-of-mass effects as explained in the main text.

AZ	J^π	E_{ex}^c [MeV]	I_c^π	nlj	C^2S	σ_{abs} [mb]	σ_{diff} [mb]	σ_{coul} [mb]	$\sigma(I_c^\pi)$ [mb]		
${}^7\text{Be}$	$3/2^-$	g.s.	1^+	$1p_{3/2}$	0.368	20.3	16.9	1.0	38.2		
				$1p_{1/2}$	0.306	16.0	13.1	0.8	29.9		
		2.186	3^+	$1p_{3/2}$	0.365	18.0	14.3	0.5	32.8		
$\sigma_p^{Glauber}=117$ mb											
${}^{10}\text{B}$	3^+	g.s.	$3/2^-$	$1p_{3/2}$	1.097	29.3	24.6	2.30	56.2		
				$\sigma_p^{Glauber}=62$ mb							
${}^{11}\text{C}$	$3/2^-$	g.s.	3^+	$1p_{3/2}$	0.927	16.8	13.5	0.8	31.1		
				1^+	$1p_{3/2}$	0.756	13.2	10.5	0.5	24.2	
					$1p_{1/2}$	0.532	8.6	6.8	0.3	15.8	
$\sigma_p^{Glauber}=78$ mb											
${}^{12}\text{N}$	1^+	g.s.	$3/2^-$	$1p_{3/2}$	0.073	3.3	3.4	2.0	8.8		
				$1p_{1/2}$	0.518	21.6	22.5	13.5	57.7		
				$2p_{3/2}$	0.001	0.07	0.07	0.04	0.2		
				$2p_{1/2}$	0.002	0.13	0.14	0.08	0.35		
				2.000	$1/2^-$	$1p_{3/2}$	0.302	8.9	8.5	2.3	19.7
						$1p_{1/2}$	0.038	1.0	0.9	0.3	2.2
				4.318	$5/2^-$	$1p_{3/2}$	0.130	2.9	2.6	0.40	5.9
						$3/2^-$	$1p_{3/2}$	0.085	1.8	1.6	0.2
				$1p_{1/2}$	0.538		10.8	9.2	1.2	21.2	
				$2p_{3/2}$	0.001		0.04	0.03	0.0	0.07	
$2p_{1/2}$	0.002	0.08	0.06	0.01	0.14						
$\sigma_p^{Glauber}=130$ mb											
${}^{13}\text{O}$	$3/2^-$	g.s.	1^+	$1p_{3/2}$	0.086	3.4	3.4	1.03	7.83		
				$1p_{1/2}$	0.537	19.3	19.1	5.84	44.24		
$\sigma_p^{Glauber}=56$ mb											
${}^{15}\text{O}$	$1/2^-$	g.s.	1^+	$1p_{3/2}$	0.372	6.5	5.5	0.65	12.65		
				$1p_{1/2}$	0.606	9.7	8.1	0.98	30.45		
$\sigma_p^{Glauber}=46$ mb											